JOURNAL OF AIRCRAFT
Vol. 48, No. 3, May–June 2011

Improvement of Unstructured Computational Fluid Dynamics Simulations Through Novel Mesh Generation Methodologies

Simone Crippa*
DLR, German Aerospace Center, 38108 Braunschweig, Germany

DOI: 10.2514/1.C031219

On the basis of the DLR, German Aerospace Center contribution to the fourth AIAA Drag Prediction Workshop, a procedure is documented to produce an unstructured grid family as self-similar as possible, with a specific procedure for steering the near-field advancing-layer process. A novel hybrid mesh generation approach is presented, in which adjoint-based dissipation error evaluations are successfully employed to improve the solution accuracy for specific conditions. An intrinsic deficit of the standard mesh generation procedure results in an unsatisfying resolution of flow features at the wing–body junction. For this case, a solution strategy based on chimera grids is tested and found to improve the aerodynamic evaluation.

I. Introduction

THE successful drag prediction workshop series set the focus of its fourth gathering (DPW4) in the blind prediction of drag and pitch moment coefficients of the NASA common research model (CRM) [1] transonic wing–body–tail (WBT) configuration. One of the main objectives of DPW4 was to evaluate the performance of state-of-the-art computational fluid dynamics (CFD) codes. This study documents some of the steps undertaken at the Institute of Aerodynamics and Flow Technology of the DLR, German Aerospace Center (DLR) to prepare the contribution for DPW4. To identify possible CFD areas needing additional research and development, both standard procedures were used in this study and advanced methodologies, such as new grid generation methods and advanced turbulence models.

The CFD solver employed for this study, the DLR TAU code [2], is used here in conjunction with the most widely used one- and two-equation turbulence models [Spalart–Allmaras (SA) [3] and Menter shear stress transport (SST) k-ω [4]] but also with the Speziale–Sarkar–Gatski/Launder–Reece–Rodi (SSG/LLR-ω) differential Reynolds stress model (RSM) [5].

The hybrid quad-dominant grid generation package Solar [6] is mainly used in the semiautomated mode, whereby the geometry of the configuration at hand is subdivided into several zones of either lifting surfaces or bodies. Afterward, a set of volume sources are automatically distributed for each component according to so-called philosophy files in which accumulated knowledge and best-practice guidelines are collected. To achieve an optimal discretization for the DPW4 contribution, these sources are then modified and manually complemented in certain regions of interest.

The DPW committee releases a set of guidelines to guarantee similar grid quality for all workshop contributions.[†] In some points, the guidelines discern between structured and unstructured grids. This is necessary, as the generation of a family of truly self-similar unstructured grids is not possible with the standard advancing-layer/advancing-front approaches. One of the key design features of Solar can be used to achieve a high level of self-similarity between the grid levels. Only one set of volumetric, background sources are used to steer the complete mesh generation process. An influence on the complete grid (surface and volume) is achieved by appropriately scaling only the target spacing of these sources.

The complete DPW4 data set produced by DLR is the basis for a detailed aerodynamic assessment by Brodersen et al. [7]. A subset of the data is used here to elucidate on the preworkshop grid generation procedure and a postworkshop discretization improvement effort.

II. Case and Grid Descriptions

During the initial grid evaluation process, it became clear that the sharp ending of the body tail cone onto the symmetry plane is detrimental to the convergence of the available RSMs. The precise reason for this is not understood yet, but a workaround is found by slightly modifying the tail cone trailing edge. The sharp trailing edge is cut off at $x = 2561.5$ in., resulting in a blunt trailing edge of 0.5 in. thickness. For the sake of consistency, the modified geometry is used for all cases/computations.

Because of the advancing-layer approach used in Solar, in concave corners, the wall-normal extrusion of the surface mesh may result in layer intersections. To avoid these intersections, the expansion ratio is locally reduced, which leads to a local contraction of the prismatic/hexahedral layer. If the spanwise spacing at the wing and tail root is too small, the contraction of the layer may be so extreme that the boundary-layer edge in the concave corner is not resolved with prisms/hexahedra. Therefore, the chosen spanwise spacing is higher than the value given in the gridding guidelines. For the medium grid of the family of self-similar grids used for a grid convergence study, the spanwise spacing at the root is approximately 0.8% local semispan, where the gridding guidelines require a value of 0.1%. A possible alleviation of the detrimental layer contraction is discussed in Sec. IV.

The full contribution of DLR to DPW4 covers three of the four cases defined by the DPW committee (cases 1.1, 1.2, and 3) requiring, in total, seven separate grids. Case 3 is not part of this study.

A. Case 1.1

Case 1.1 refers to the grid convergence study, performed on the WBT CRM configuration with the tail deflection angle ih of 0°. The far-field conditions are Mach 0.85 and a Reynolds number of 5,000,000, based on the reference chord of 275.80 in. The angle of attack has to be adapted to achieve a constant lift coefficient of 0.5.

For a grid convergence study, at least three grids with varying discretizations are required to determine the order of convergence and to perform Richardson extrapolation. At the given flow conditions, all three grids belonging to the grid family have to lie

Presented as Paper 2010-4672 at the AIAA Applied Aerodynamics Conference: CFD Drag Prediction Workshop Results, Chicago, IL, 28 June–1 July 2010; received 23 August 2010; revision received 24 November 2010; accepted for publication 15 December 2010.

*Research Scientist, Institute of Aerodynamics and Flow Technology, $C^2A^2S^2E$, Lilienthalplatz 7. Member AIAA.

[†]Data available at http://aaac.larc.nasa.gov/tsab/cfdlarc/aiaa-dpw/Workshop4/gridding_guidelines_4.html [retrieved 12 August 2010].

Table 1 Overall grid details for case 1.1

	Grid		
	Coarse	Medium	Fine
Surface points	$130 \cdot 10^3$	$271 \cdot 10^3$	$566 \cdot 10^3$
No. of points in prism/hexalayer	$3.47 \cdot 10^6$	$9.94 \cdot 10^6$	$28.69 \cdot 10^6$
No. of tetrahedral cells	$5.31 \cdot 10^6$	$14.31 \cdot 10^6$	$38.58 \cdot 10^6$
Total no. of points	$4.07 \cdot 10^6$	$11.70 \cdot 10^6$	$34.08 \cdot 10^6$
Total grid size ratio (medium grid as reference)	1/2.87	1	2.91
Total no. of cells	$8.56 \cdot 10^3$	$23.78 \cdot 10^6$	$66.65 \cdot 10^6$

Table 2 Near-field grid details

	Grid		
	Coarse	Medium	Fine
First wall-normal layer spacing a	$1.478 \cdot 10^{-3}$ in.	$9.85 \cdot 10^{-4}$ in.	$6.57 \cdot 10^{-4}$ in.
No. of cells with constant spacing	3	3	3
Expansion ratio q	1.3009	1.2	1.135
Max. no. of wall-normal layers N	30	42	60

within the asymptotic range of convergence; this implies that all relevant aerodynamic phenomena have to be resolved on all three levels. For the three required grid levels (coarse, medium, and fine), the guidelines call for a ratio of three in the total number of points between two levels. Because of the requirement in Solar to specify the target grid spacing in distinct volume sources, a one-dimensional refinement/coarsening factor is required. A factor of three for a three-dimensional grid translates to a one-dimensional scaling factor r of $\sqrt[3]{3}$, or approximately 1.4422. Only this factor is used to scale the volumetric sources, whereas the range of influence of the sources is not changed, as it is linked to the geometry. A further requirement of the gridding guidelines sets the minimal resolution across the thick trailing edges of the lifting surfaces. To comply with this requirement, the three grids prepared for the workshop feature 8, 12, and 18 cells across the trailing edges. A summary of the final grid family point and element counts is given in Table 1.

The input values required by the advancing-layer grid generation process, the first layer spacing, and the expansion ratio have to be chosen wisely. During the grid generation and evaluation process for DPW4, it was discovered that a similar total layer thickness between the grid levels is of paramount importance for a successful, unstructured grid convergence study. It is important to resolve the same physical region on the various grid levels with the same element types. A similar near-field extent normal to the walls guarantees that the transition location from prismatic/hexahedral elements to tetrahedral is similar between the grid levels. If the transition between different element types is located in the same physical region, eventual discretization errors are located similarly on all grid levels.

The relations between the grid levels in terms of first layer spacing and number of wall-normal layers should follow the preceding scaling factor. Given the requirement for a self-similar total layer thickness, the scaled first layer spacing and scaled total number of layers leaves only the expansion ratio as a variable to be determined. The geometric series for the total layer thickness H is

$$H = \sum_{i=0}^{n} a \cdot q^i = a \cdot \frac{1 - q^{n+1}}{1 - q} \tag{1}$$

where the total number of layers is $N = n + 1$, the expansion ratio is q, and the first layer spacing is a. Keeping the total layer thickness between two grid levels constant ($H_1 = H_2$) results in

$$a_1 \cdot \frac{1 - q_1^{N_1}}{1 - q_1} = a_2 \cdot \frac{1 - q_2^{N_2}}{1 - q_2} \tag{2}$$

Hereby, the relation between a_1 and a_2, as well as N_1 and N_2, is set by the scaling factor $r = \sqrt[3]{3}$; for example, with grid level 2 being finer than grid level 1, it follows that $a_2 = a_1/\sqrt[3]{3}$ and $N_2 = N_1 \cdot \sqrt[3]{3}$. Please notice that, for N_2, an integer value has to be used due to the nature of the advancing-layer process. Thus, starting with a sensible value for the expansion ratio q_1 and a total number of layers N_1, the only unknown in Eq. (1) is q_2, which can be computed iteratively.

If the scaling factor allows for integer values for the total number of layers, and if the scaling factor is the same for the first cell height and number of layers, then the relation of the expansion factors is approximately $q_2 = q_1^{1/r}$. Although the prerequisites are not met here, using this approximation would lead to a minor difference in terms of q. The difference in total layer height would then be of 1 or 5%, respectively, for the fine and coarse grids, compared with the total layer height of the medium grid.

For the DPW4 family of grids, the values for the coarse and fine levels are derived from the medium grid. The first layer spacings dictated by the gridding guidelines are used, as the scaling factor of 1.5 is sufficiently close to $\sqrt[3]{3}$. The resulting values for the near-field mesh are summarized in Table 2. Note that, for full consistency, the number of initial wall-normal layers with constant spacing should also be scaled by $\sqrt[3]{3}$, but neglecting this has an irrelevant effect on total layer height and was not found to influence the results. Furthermore, note that the expansion ratios of Table 2 fulfill the requirement given in the gridding guidelines for only the medium and fine grids. The expansion ratio of the coarse grid is larger than the required value of 1.25.

A comparison of the three final grids is shown in Fig. 1, where the approximate self-similarity between the three levels is visible in the highlighted region. In the wall-tangential direction, the factor of approximately 1.5 can be recognized by the cascade of 2, 3, and 4.5 quadrilateral elements. A similar wall-normal total layer extent is also recognizable.

B. Case 1.2

Case 1.2 refers to a trim drag analysis by variation of the horizontal tail deflection angle between −2, 0, and 2°. The far-field conditions are the same as for case 1.1, only an angle-of-attack sweep from 0 to 4° is performed for each of the three WBT configurations and a configuration without tailplane (WB). The configuration with a tail deflection angle of 0° (WBT $ih = 0°$) is identical to the configuration of case 1.1. For the other two WBT configurations, the same Solar background sources as for the WBT $ih = 0°$ configuration are used. The sources of the horizontal tail are rotated according to the

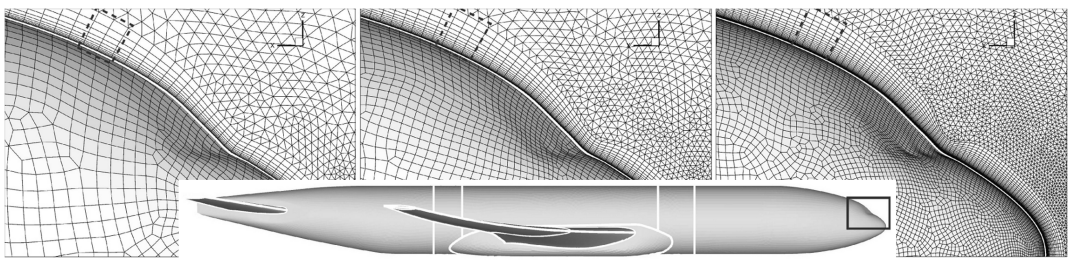

Fig. 1 Comparison of coarse, medium, and fine grids (left to right); lateral view on forebody and symmetry plane.

Table 3 Overall grid details for case 1.2

	Grid			
	WB	WBT $ih = -2°$	WBT $ih = 0°$	WBT $ih = +2°$
Surface points	$208 \cdot 10^3$	$271 \cdot 10^3$	$271 \cdot 10^3$	$271 \cdot 10^3$
Max. no. of wall-normal layers	43	42	42	42
No. of points in prism/hexalayer	$7.32 \cdot 10^6$	$9.94 \cdot 10^6$	$9.94 \cdot 10^6$	$9.94 \cdot 10^6$
No. of tetrahedral cells	$4.62 \cdot 10^6$	$12.76 \cdot 10^6$	$14.31 \cdot 10^6$	$14.65 \cdot 10^6$
Total no. of points	$8.59 \cdot 10^6$	$11.45 \cdot 10^6$	$11.70 \cdot 10^6$	$11.71 \cdot 10^6$
Total no. of cells	$17.29 \cdot 10^3$	$22.24 \cdot 10^6$	$23.78 \cdot 10^6$	$24.1 \cdot 10^6$

geometric deflection angle ($ih = -2$ or $2°$) or neglected altogether for the WB configuration. The resulting grid sizes are summarized in Table 3. For the scope of this study, only a subset of the CFD data is used, namely, the data at the angle of attack of 4° for the WBT $ih = 0°$ configuration.

III. Detailed Grid Analysis and Improvement

An initial grid family for case 1.1 was generated using Solar standard procedures. For the initial grid family, the main improvement from the standard procedure consists of adding a chordwise refinement at the wing midchord over the entire span. After checking the grid convergence behavior of the initial grid family, an improvement with the discrete adjoint solver available in the TAU code [8] was sought. The error due to dissipation is evaluated on the initial medium grid for two adjoint functionals: drag and pitch moment coefficients. The employed adjoint evaluation detects only the sources of error due to second- and fourth-order dissipation of the employed Jameson–Schmidt–Turkel [9] artificial viscosity scheme. The error due to dissipation has been shown [10] for two transonic (inviscid) test cases to account for more than 90% of the total error of integrated forces. The errors due to artificial dissipation should decrease with finer grids, up to the theoretical limit of grid converged solutions where the error due to dissipation would vanish. The adjoint solver does not only output the total error estimate of the evaluated cost function but also the scaled contribution of each cell. The local error variable scaled by the cell volume (adjoint-V4) is used to visually assess if the initial source distribution and spacing is appropriate throughout the field. By visualizing the cells with a local error variable higher than a reasonable threshold, several regions can be identified that have a major contribution to the total error. Some of the regions identified during interactive postprocessing are visible in Fig. 2. A clustering of cells with larger local error variable are found 1) upstream of the entire wing; 2) just upstream of the junction of body and wing leading edge; 3) above the model, approximately at the location of the wing–body (WB) junction, up to the wing midspan; 4) in the wingtip wake; 5) beside the fuselage, between the wing and the tailplane; 6) below and downstream of the aftbody cone; 7) in the upper and lower tailplane–body junctions from leading to trailing edges; and 8) on the upper side of the WB junction from leading to trailing edges.

To improve the grid in the insufficiently discretized regions, the source target sizes are locally decreased: for example, downstream of the wingtip to better resolve the wingtip vortex. After identifying the

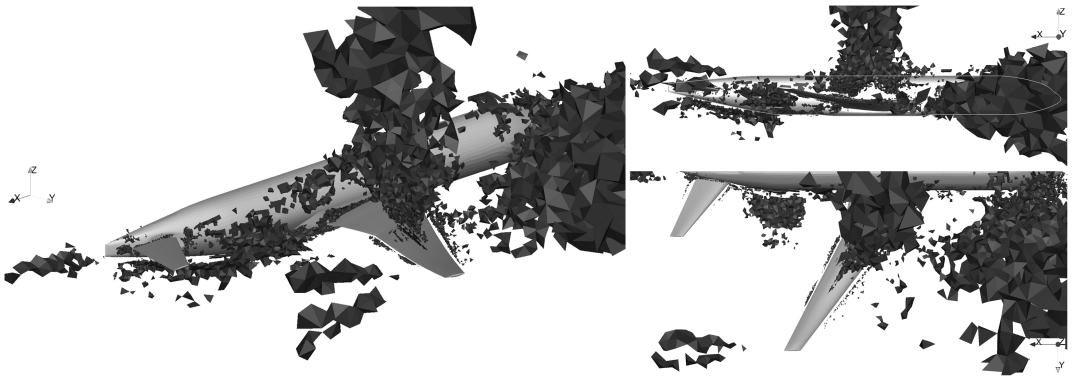

Fig. 2 Case 1.1, medium grid: cells with a local error of pitch moment coefficient larger than $1.5 \cdot 10^{-7}$. Isometric/upstream, lateral ($y-$), and top ($z-$) views.

Fig. 3 Case 1.1 medium grid: field elements of local dissipation error of pitch moment coefficient larger than $1.5 \cdot 10^{-7}$ (bottom) and drag coefficient larger than $7 \cdot 10^{-9}$ (top). Top view.

problematic regions not known a priori, new sets of sources are necessary: for example, upstream of the wing.

Because of the a priori refinement of the wing midchord, the adjoint dissipation error assessment shows that this region is indeed sufficiently discretized in the vicinity of the viscous surface. Above the viscous surface, the tetrahedra quickly increase in size, which might explain why the interaction between the shock and the fuselage is not sufficiently resolved and is thus flagged by the adjoint dissipation error evaluation. Upstream of the wing, next to the model forebody, it is possible to identify a region of information transport from the far field to the wing attachment line. This is a typical region identified by adjoint-based error indicators. In analogy to the region upstream of the wing, the region between the wing trailing edge and the horizontal tailplane also has to be refined to convect the influence of the wing onto the horizontal tailplane. The problematic WB and tailplane–body junctions are not easily recognizable in Fig. 2, but further discussion follows in the next section.

The field distribution of the discretization error variable for the pitch moment coefficient shows similar problematic regions as for the drag coefficient, although with higher absolute values of the error; see Fig. 3. This is consistent with the conjectured higher sensitivity to discretization errors of the pitch moment coefficient compared with the drag coefficient.

A significant topological difference between the two evaluations is only found with respect to the surface discretization and the corresponding first few wall-normal cells. Figure 4 shows the relative sensitivity to the same surface discretization for the two cost functions. As the image shows the error for both cost functions on the same scale, it is possible to identify for the pitch moment coefficient a main error contribution from the forebody and aftbody. This is understandable, as the front and rear part of the body contribute with a longer moment arm to the integrated value of the pitch moment coefficient. A small error in these regions has a larger effect on the pitch moment coefficient than on the drag coefficient. The relatively higher pitch moment sensitivity to the main wing shock resolution is also discernible.

The preceding detailed adjoint solution analysis is used to manually adapt and complement the initial sources for the final grid family. Through the adjoint-based field analysis, it is also possible to identify regions where the cell spacing is too small. Thus, it is possible to perform a tradeoff evaluation in terms of dissipation, and grid discretization error, and limit the increase of total grid points to approximately 10% for the medium grid. The modification of the background sources is only performed for the medium grid; the fine and coarse grids are then derived from it.

The grid convergence of the drag and pitch moment coefficient for the two grid families (initial and final) is plotted versus the grid index factor in Fig. 5. The grid index factor is the inverse of the total number of points to the power of $2/3$ ($N^{-2/3}$). The graphs in Fig. 5 also depict the theoretical second-order convergence line extracted from the medium- and fine-grid values, assuming that only the coarse grid is outside of the asymptotic range of convergence. This allows us to appreciate the relative improvement between the initial and final grid families.

Given a set of three-dimensional self-similar grids with the same relative difference in total grid points, global solution quantities of a numerical scheme of formally second-order accuracy are expected to lie on a straight line when plotted versus the chosen grid index factor. A deviation from linear convergence in this coordinate system can be attributed to different global flow resolution between the grid levels. A slight deviation is also possible when local flow feature differences appear between the different grids.

From Fig. 5a, it is possible to recognize that the grid convergence rate for the drag coefficient of the final grid family is nearly linear. The drag coefficient convergence rate for the initial grid family is higher than second order. The same is true for both pitch moment convergence curves (see Fig. 5b), but a relative difference is difficult to discern.

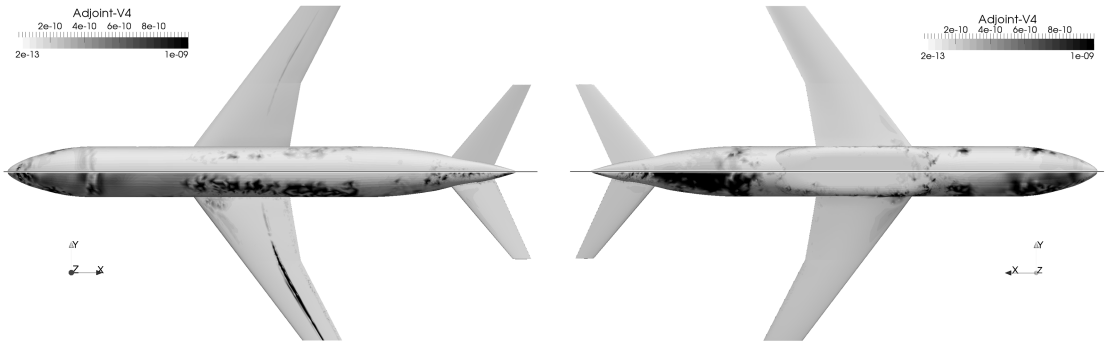

a) View from above **b) View from below**

Fig. 4 Case 1.1, medium grid: local dissipation error of pitch moment (lower model half) and drag (upper model half) coefficients on surface elements.

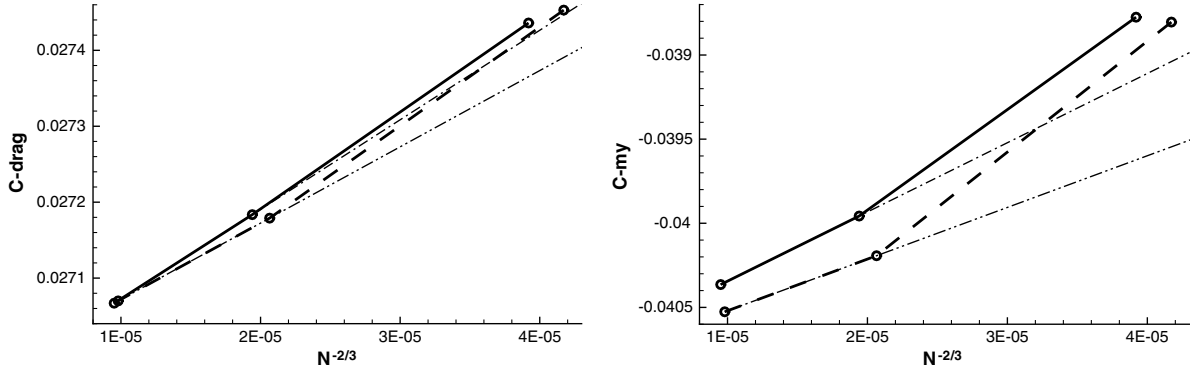

a) Drag coefficient (C-drag) **b) Pitch moment coefficient (C-my)**

Fig. 5 Case 1.1 grid convergence for the initial (dashed lines) and final (solid lines) grid families: second-order convergence rate between medium and fine grid solutions is sketched for each family (dashed–dotted lines).

Table 4 Drag and pitch moment coefficient values for the coarse grid

	Initial family			Final family		
	Computed value	Ideal value	Difference	Computed value	Ideal value	Difference
C_{drag}	$2.7453 \cdot 10^{-2}$	$2.7391 \cdot 10^{-2}$	$6.2345 \cdot 10^{-5}$	$2.7436 \cdot 10^{-2}$	$2.7417 \cdot 10^{-2}$	$1.9064 \cdot 10^{-5}$
C_{my}	$-3.8804 \cdot 10^{-2}$	$-3.9546 \cdot 10^{-2}$	$7.4154 \cdot 10^{-4}$	$-3.8775 \cdot 10^{-2}$	$-3.9143 \cdot 10^{-2}$	$3.6760 \cdot 10^{-4}$

At the same grid index factor as for each coarse-grid solution, the ideal value can be extracted from the linear medium-fine prolongation line. The relative improvement between the two sets of grid families can thus be quantified as the ratio between the two coarse-grid deviations from the second-order convergence rate in either the drag or pitch moment coefficient. The computed values for the two coefficients, along with the ideal values at the same grid index factor, are given in Table 4. The relative improvement is approximately a factor of 3.3 for the drag coefficient and 2.0 for the pitch moment coefficient.

IV. Discretization Improvement Through Chimera Technique

At the DPW4 held in San Antonio, TX, 20–21 June 2009, a majority of the participants detected small separated regions at the trailing edge of the wing and tailplane junctions with the body [11]. The existence or absence of the separation bubbles was found to be neither coupled to a solver type (unstructured or structured) nor a specific physical modeling approach. The results on the Solar grids from two participants using, in total, four different turbulence models, did not feature these small separations.

An insight gained through the adjoint dissipation error evaluation is that the WB and tailplane–body junction regions are not sufficiently well discretized. This is only partially visible in Fig. 2. The spanwise field cut at $x = 1429$ in. (wing–body junction), shown in Fig. 6, reveals that the contracted near-field mesh leads to very large tetrahedra in the concave corners that are not adequate to resolve the edge of the boundary layer. The interface between prism/hexalayers and tetrahedral elements is marked by the solid line on the field cut plane, which is colored by the local dissipation error of drag coefficient. Cells with a local error of drag coefficient larger than $7 \cdot 10^{-9}$ are visible upstream of the cut plane. The cells between the line of sight and the cut plane are rendered transparently for improved view on the cut-plane.

A way to alleviate this problem, as described in Sec. II, is to increase the spanwise spacing at the junction; however, the procedure is not sufficient to fully resolve the problem. The grids for the DPW4 contribution were known to be affected by the junction layer contraction, but a simple solution to this problem is not known. A solution is sought on the solver side, as the near-field layer contraction in these concave regions cannot be completely excluded from the Solar grid generation process.

Schwarz [12] has recently implemented in the TAU code the capability to compute on chimera (overset) grids with overlapping viscous boundaries. A fully hexahedral grid was generated with a C-H topology around the complete wing airfoil and some of the wake at the wing root; see Fig. 7.

The grid spacing in the overlap/interpolation region is similar to the medium Solar grid, but the resolution at the WB junction is improved due to the chosen H topology, as opposed to an O-grid topology. The additional hexahedral grid features 5,251,719 points, 5,140,736 elements with 391 points on the upper and lower wing airfoils, 74 points normal to the wing, 129 points normal to the body,

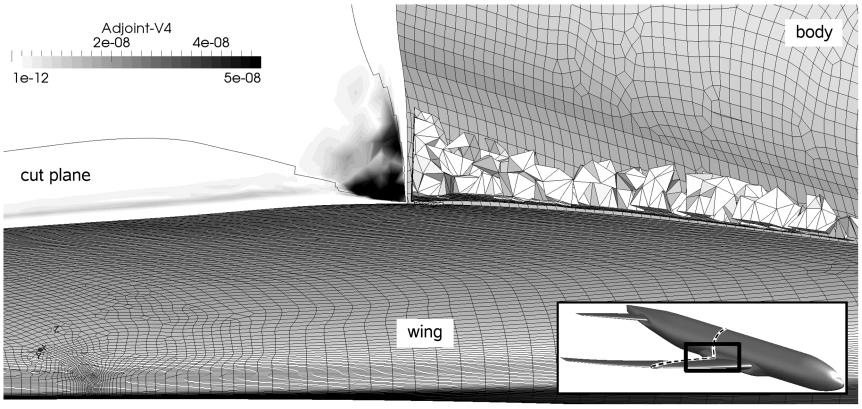

Fig. 6 Case 1.1, medium grid: local dissipation error of drag coefficient: isometric/downstream view.

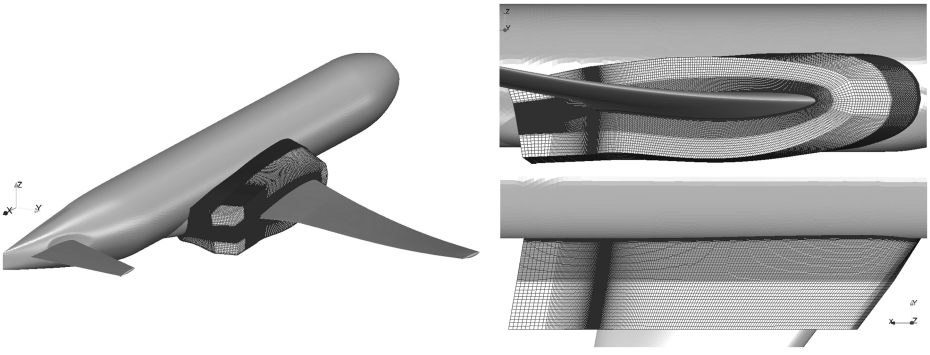

Fig. 7 Additional hexahedral block. Isometric/upstream, lateral, and top views.

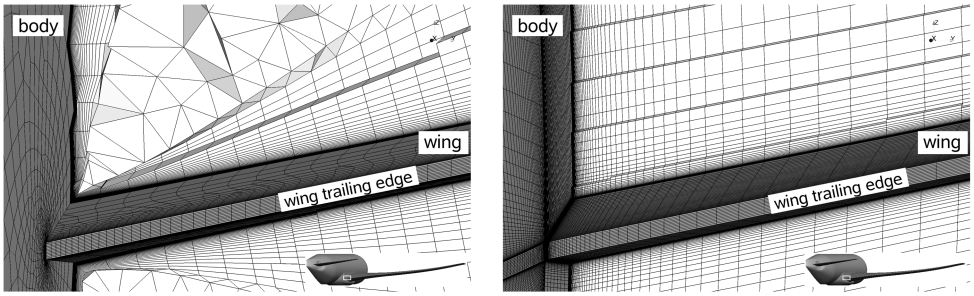

a) Solar grid b) SolarChimera5 grid

Fig. 8 Comparison of SolarChimera5 and Solar medium grids at $x = 1454$ in. plane: viscous wall surfaces in dark gray, field cut in white (upstream view on the WB junction at the trailing edge).

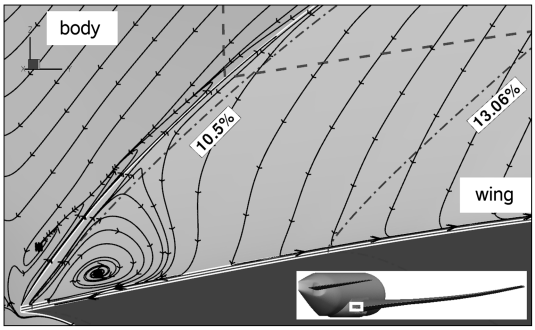

Fig. 9 Skin-friction lines $c_{p,\text{crit}}$ (dashed lines) and selected surface cut planes (dashed–dotted lines): SolarChimera5 grid (upstream view on the WB junction at the trailing edge).

and 13 points (12 elements) across the blunt trailing edge. Hereafter, the chimera grid composed of the case 1.1 medium grid and the approximately 5,000,000-element hexahedral grid is referred to as SolarChimera5, whereas the initial medium grid is referred to plainly as Solar. The different viscous surface and field discretizations of the Solar and SolarChimera5 grids at the WB junction are compared in Fig. 8. The prism/hexalayer contraction toward the WB junction of the Solar grid (Fig. 8a) requires the insertion of large tetrahedra. The H-type field discretization at the junction, shown in Fig. 8b, should be better suited to resolve the boundary layers on body and wing and their interaction.

A. Case 1.1: Target-Lift Coefficient of 0.5

The solution with SA on the SolarChimera5 grid (see Fig. 9) using the same far-field settings as the plain Solar grid reveals a separation pattern similar to those observed by other DPW4 participants. In the SolarChimera5 result, the center of the separation bubble on the upper wing surface is found approximately at $x = 1454$ in., $y = 124$ in.

By plotting the critical pressure coefficient $c_{p,\text{crit}}$, as in Fig. 9, it is possible to identify the sonic line impinging on the corner boundary layer. The sonic line is found at $x/c_{\text{root}} \approx 0.74$, with a wing root chord c_{root} of 466 in. The separation bubble in the junction starts upstream of the shock at $x/c_{\text{root}} \approx 0.68$, and it remains at first constrained to a small region in the corner up until $x/c_{\text{root}} \approx 0.86$, where it expands substantially.

The relatively small extent of the separation bubble is appreciated when considering that the first spanwise experimental pressure tap row is located at the nondimensional wing half-span (η) section of 13.06%. This innermost pressure tap row, in complement to surface flow visualizations, is intended to detect the possible junction flow separation in the wind-tunnel campaign. Unfortunately, the tap row at $\eta = 13.06\%$ is outside of the immediate influence region of the separation bubble. Although the solutions on the Solar and SolarChimera5 grids differ in respect to the existence of the junction separation bubble, a difference is not detectable at $\eta = 13.06\%$; see Fig. 10. Both pressure and skin-friction coefficients on the upper wing surface can not be clearly discerned from each other.

For the numerical results of DPW4, the innermost data extraction cut plane is at $\eta = 10.5\%$, which is located between the junction and the separation bubble eye. The separation at the trailing edge is clearly detected through the negative skin-friction coefficient for the SolarChimera5 grid (see Fig. 11b). Furthermore, the comparison in terms of skin-friction coefficient shows a difference along the entire chord, and not only at the trailing edge. This may suggest an already insufficient resolution from the leading edge. In terms of pressure coefficient (see Fig. 11a), the difference between the results on the two grids is not as pronounced. Even after the shock, toward the

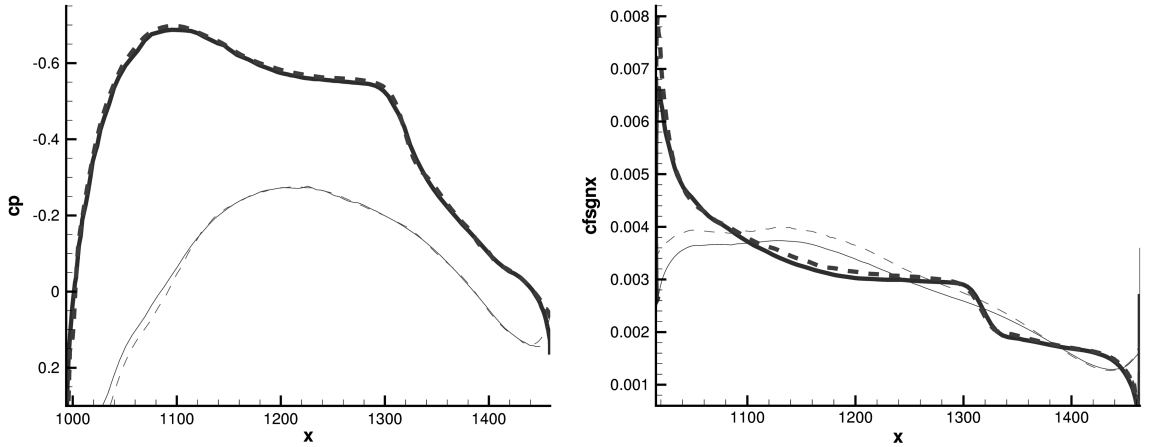

a) Pressure coefficient (cp) b) Skin-friction coefficient, multiplied by the sign of the x component of skin friction (cfsgnx)

Fig. 10 Case 1.1 $Cl = 0.5$ wing cut at $\eta = 13.06\%$: upper wing surface (bold curves), Solar (solid lines), and SolarChimera5 (dashed lines) SA results.

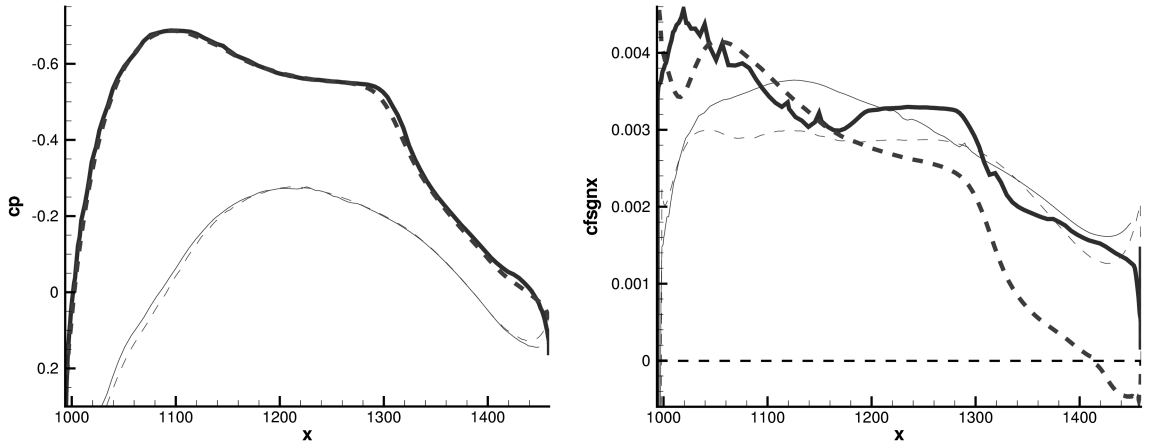

a) Pressure coefficient (cp)

b) Skin-friction coefficient, multiplied by the sign of the x component of skin friction (cfsgnx)

Fig. 11 Case 1.1 $Cl = 0.5$ wing cut at $\eta = 10.5\%$: upper wing surface (bold curves), Solar (solid lines), and SolarChimera5 (dashed lines) SA results.

trailing edge, a striking difference between the two results is not found. Note that, due to the small three-dimensional extent of the separated region, a clear sign of separation is not noticeable solely from surface pressure data.

The comparison between SA, Menter SST, and RSM in Fig. 12a shows virtually no difference in pressure coefficient. The levels of skin-friction coefficient (Fig. 12b) are slightly different, but the overall trend is the same. The skin-friction coefficient curves show a

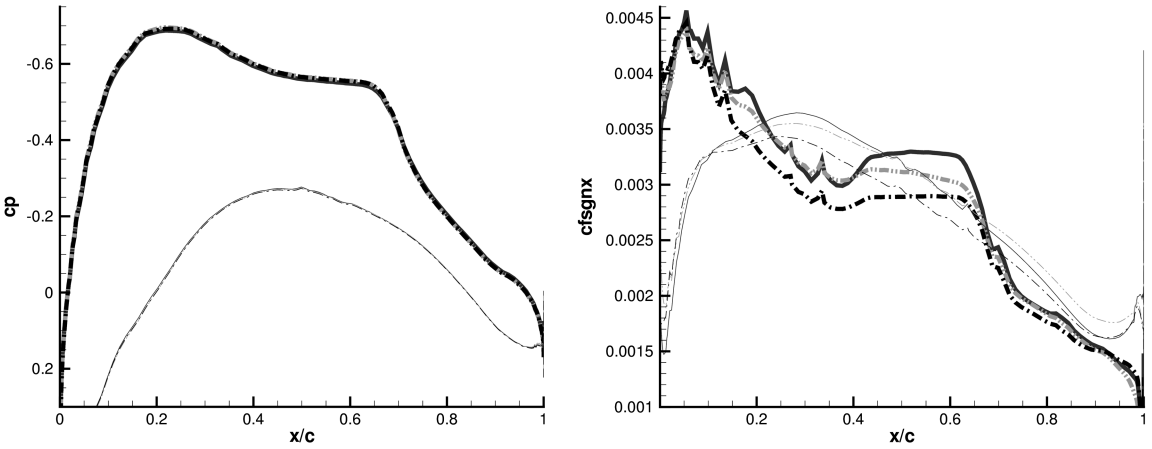

a) Pressure coefficient (cp)

b) Skin-friction coefficient, multiplied by the sign of the x component of skin friction (cfsgnx)

Fig. 12 Case 1.1 $Cl = 0.5$ wing cut at $\eta = 10.5\%$: upper wing surface (bold curves), SA (solid lines), SST (dashed–dotted–dotted lines), and RSM (dashed–dotted lines) results on Solar grid.

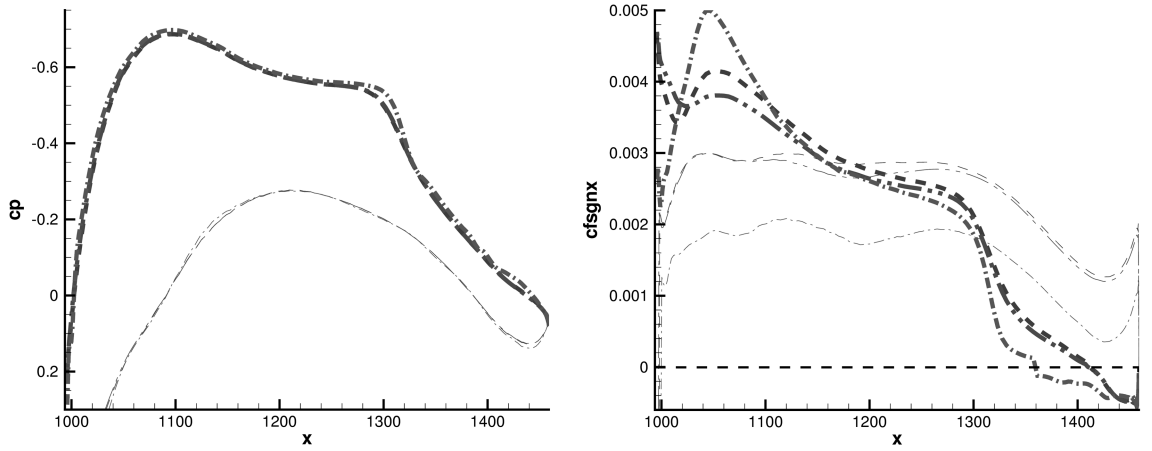

a) Pressure coefficient (cp)

b) Skin-friction coefficient, multiplied by the sign of the x component of skin friction (cfsgnx)

Fig. 13 Case 1.1 $Cl = 0.5$ wing cut at $\eta = 10.5\%$: upper wing surface (bold curves), SA (dashed lines), SARC (dashed–dotted–dotted lines), and RSM (dashed–dotted lines) results on SolarChimera5 grid.

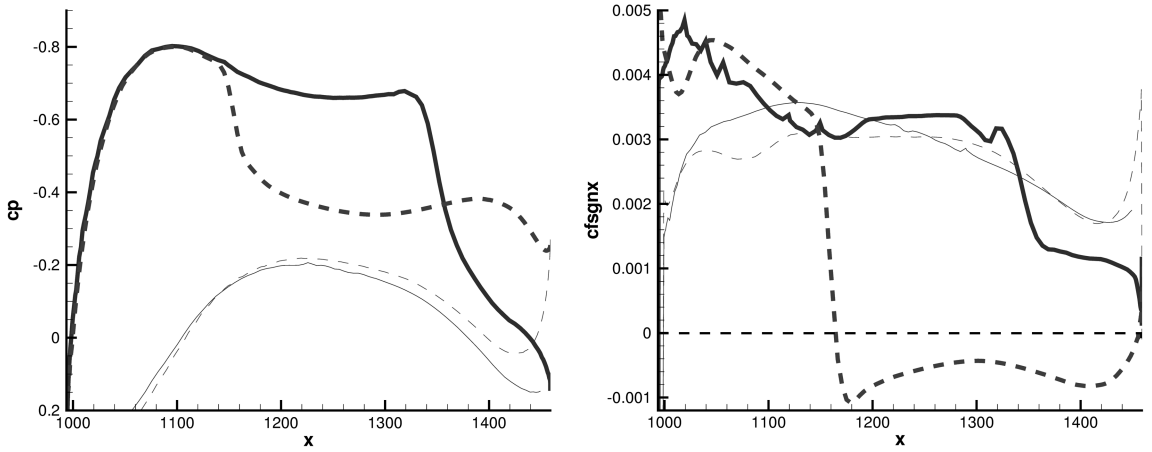

a) Pressure coefficient (cp)

b) Skin-friction coefficient, multiplied by the sign of the x component of skin friction (cfsgnx)

Fig. 14 Case 1.2 $\alpha = 4°$ wing cut at $\eta = 10.5\%$: upper wing surface (bold curves), Solar (solid lines) and SolarChimera5 (dashed lines) SA results.

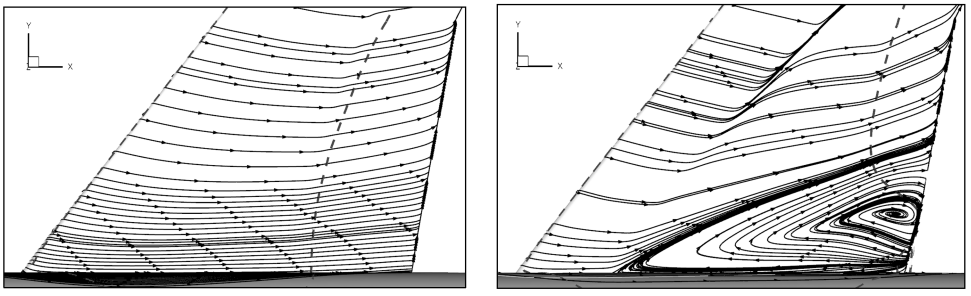

a) Solar

b) SolarChimera5

Fig. 15 Case 1.2 $\alpha = 4°$: top view of skin-friction lines on inner wing and $c_{p,\text{crit}}$ (dashed lines); SA result.

similar behavior upstream of the shock, a postshock dropoff to comparable levels, and no separation at the trailing edge. More advanced physical models do not improve the situation on the Solar grid.

A similar turbulence model comparison on the SolarChimera5 grid also shows a negligible dependence on physical modeling. The comparison depicted in Fig. 13 shows that various turbulence models behave in a similar way. The difference in skin friction at the leading edge between the SA and RSM solutions does not affect the region around the shock wave. The RSM result shows a more pronounced separation due to a stronger effect of the shock wave on the boundary layer, but the separation bubble is topologically similar to the SA solution. Additional rotation and curvature corrections to the SA model (SARC) are conjectured to influence the trailing-edge separation through better resolution of the horseshoe vortex that develops at the junction of wing leading edge and fairing. An effect of the improved rotational flow modeling is indeed found at the leading edge, but an influence on the separation bubble is not observed.

B. Case 1.2: Edge of Envelope

A further comparison is performed at an offdesign condition between the Solar grid and the SolarChimera5 grid. At a target lift of 0.5 for case 1.1, the angle of attack is approximately 2.3°. At angles of attack above 3°, the spread in terms of drag and pitch moment coefficients of all DPW4 participants increases dramatically compared with the target-lift case [11]. This is partly due to a major difference between the contributions in respect to WB separation. The results show attached flow on the Solar grid at an angle of attack α of 4°, regardless of the turbulence modeling approach (SA, SST, and RSM). At the same angle of attack, the SolarChimera5 results for SA show a major separation; see Fig. 14. The skin-friction coefficient plot at $\eta = 10.5\%$ (Fig. 14b) suggests fully attached flow for the Solar result, with a similar trend as for case 1.1. The SolarChimera5 result shows reversed flow for a major portion of the cut. The pressure coefficient plot (Fig. 14a) shows considerable differences between the two results, as opposed to case 1.1.

The separation in the SolarChimera5 solution, which for case 1.1 is seemingly confined at the trailing edge, moves upstream and starts at $x/c_{\text{root}} \approx 0.35$. The flowfield of the inner wing section up to the kink is dominated by a substantial separation; see Fig. 15.

V. Conclusions

This study documents a large amount of the grid generation efforts undertaken at DLR with the Solar meshing system for the DPW4. The procedure described here to produce a grid family as self-similar as possible was found to improve the grid convergence behavior for unstructured solutions. It remains to be seen if the approach also proves successful in future grid convergence studies; however, within the context of DPW4, the grid convergence trends and levels compared with other DPW4 contributions are satisfactory. This is the case even if the small separation bubbles at the wing and tailplane junctions with the body are not resolved. The grid convergence is not affected, since the separation is absent on all grid levels. Fortunately, the influence of the separation bubbles on drag and pitch moment coefficients is minor at the target-lift coefficient of 0.5.

The adjoint-based dissipation error evaluations are shown to improve the hybrid CFD process accuracy through targeted grid modifications. An increase of approximately 10% in grid points was shown to improve the results of an initial family of grids toward second-order convergence. The documented procedure can already support the interactive mesh generation process. The manually performed process documented here is in the process of being automated, at first through mesh adaptation within the solver and possibly later by a direct interface to the mesh generation package.

Using the standard Solar mesh generation procedure, it is not possible to resolve a main flow feature at the WB junction. An alternative solution strategy using a chimera grid is tested and found to improve the aerodynamic evaluation. Without changing the solver settings, the separation bubble at the wing root trailing edge is resolved on the chimera grid. Therefore, the absent separation on the Solar grid is only due to insufficient discretization. An analysis of the solutions on the two grids gives some insight into the flow phenomenon at the WB junction. The pressure rise at midchord of the cut plane $\eta = 10.5\%$ is very similar between Solar and SolarChimera5 solutions; thus, the strength of the shock wave is comparable. Therefore, the boundary-layer resolution is the sole reason for the difference between the two grids. The shock-boundary-layer interaction is responsible for the initial destabilizing effect on the corner boundary layer. Only, on the SolarChimera5 grid, this interaction is shown to initialize the separation, which can subsequently enlarge at the trailing edge. A sufficient discretization is not only important downstream of the shock to resolve this phenomenon but also upstream of the shock. A correct resolution of the corner boundary layer between leading edge and shock is necessary to capture the boundary-layer development and the proper interaction with the shock wave. Using more advanced turbulence models does not compensate for the insufficient corner flow discretization. Only when the discretization is sufficient can one draw correct conclusions to classify and categorize the different physical modeling approaches.

The improvement of the corner flow discretization via the additional hexahedral mesh block shows a major impact on the flowfield at offdesign conditions. Capturing topologically correct flow features is of particular importance at offdesign. The absolute values may not be correct, but the trends of pitching moment and drag are crucial for a correct assessment of a design. The same phenomenon elucidated here on the WB junction is also found at the tailplane–body junction [12], which has even more profound effects on the pitching moment.

References

[1] Vassberg, J. C., Dehaan, M. A., Rivers, M. S., and Wahls, R. A., "Development of a Common Research Model for Applied CFD Validation Studies," 26th AIAA Applied Aerodynamics Conference, AIAA Paper 2008-6919, Aug. 2008.

[2] Schwamborn, D., Gerhold, T., and Heinrich, R., "The DLR TAU-Code: Recent Applications in Research and Industry," *Proceedings of the European Conference on Computational Fluid Dynamics, ECCOMAS CFD 2006* [CD-ROM], edited by P. Wesseling, E. Oñate, and J. Périaux, Delft Univ. of Technology, The Netherlands, 2006.

[3] Spalart, P. R., and Allmaras, S. R., "One-Equation Turbulence Model for Aerodynamic Flows," *La Recherche Aérospatiale*, Vol. 1, No. 1, 1994, pp. 5–21.

[4] Menter, F. R., "Two-Equation Eddy-Viscosity Turbulence Models for Engineering Applications," *AIAA Journal*, Vol. 32, No. 8, 1994, pp. 1598–1605.
doi: 10.2514/3.12149

[5] Eisfeld, B., "Numerical Simulation of Aerodynamic Problems with the SSG/LRR-ω Reynolds Stress Turbulence Model Using the Unstructured TAU Code," *New Results in Numerical and Experimental Fluid Mechanics VI*, Vol. 96, Notes on Numerical Fluid Mechanics and Multidisciplinary Design, Springer–Verlag, New York, 2007, pp. 356–363.

[6] Leatham, M., Stokes, S., Shaw, J. A., Cooper, J., Appa, J., and Blaylock, T., "Automatic Mesh Generation for Rapid-Response Navier–Stokes Calculations," FLUIDS 2000 Conference and Exhibit, AIAA Paper 2000-2247, June 2000.

[7] Brodersen, O., Crippa, S., Eisfeld, B., Keye, S., and Geisbauer, S., "DLR Results from the Fourth AIAA CFD Drag Prediction Workshop," 28th AIAA Applied Aerodynamics Conference, AIAA Paper 2010-4223, June 2010.

[8] Dwight, R. P., and Brezillon, J., "Efficient and Robust Algorithms for Solution of the Adjoint Compressible Navier–Stokes Equations with Applications," *International Journal for Numerical Methods in Fluids*, Vol. 60, No. 4, June 2009, pp. 365–389.
doi:10.1002/fld.1894

[9] Jameson, A., Schmidt, W., and Turkel, E., "Numerical Solution of the Euler Equations by Finite Volume Methods Using Runge–Kutta Time-Stepping Schemes," 14th AIAA Fluid and Plasma Dynamic Conference, AIAA Paper 1981-1259, 1981.

[10] Dwight, R. P., "Heuristic A Posteriori Estimation of Error due to Dissipation in Finite Volume Schemes and Application to Mesh Adaptation," *Journal of Computational Physics*, Vol. 227, No. 5, 2008, pp. 2845–2863.
doi:10.1016/j.jcp.2007.11.020

[11] Vassberg, J. C., Tinoco, E. N., Mani, M., Zickuhr, T., Levy, D. W., Brodersen, O., Crippa, S., Wahls, R. A., Morrison, J. H., Mavriplis, D. J., and Murayama, M., "Summary of the Fourth AIAA CFD Drag Prediction Workshop," 28th AIAA Applied Aerodynamics Conference, AIAA Paper 2010-4547, June 2010.

[12] Schwarz, T., "An Interpolation Method Maintaining the Wall Distance for Structured and Unstructured Overset Grids," CEAS 2009 Conference, CEAS 2009 European Air and Space Conference, Royal Aeronautical Soc., Paper 079, London, Oct. 2009.